RSC Advances

PAPER

View Article Online
View Journal | View Issue

Cite this: *RSC Adv.*, 2024, **14**, 9996

Synthesis of Os@ZIF-8 nanocomposites with enhanced peroxidase-like activity for detection of Hg^{2+}†

Zijie Wei, Cuifeng Jiang, * Jinshan Wang and Yue Chen

Received 21st December 2023
Accepted 19th March 2024

DOI: 10.1039/d3ra08723a

rsc.li/rsc-advances

Metal organic framework (MOF)-derived nanostructures display remarkable characteristics and have broad application potential. Os@ZIF-8 nanocomposites were prepared by a depositional method. The Os nanoparticles distributed on the surface of ZIF-8. The nanocomposites displayed enhanced peroxidase-like activity with smaller K_m for both 3,3′,5,5′-tetramethylbenzidine (TMB) and H_2O_2 compared to Os NPs due to the confinement effect and large surface area that ZIF-8 provided. From the average reaction rate constants obtained from three different temperatures, the activation energy values were determined. The kinetic data indicated that the Os@ZIF-8 NCs are catalytically more active than Os NPs. In addition, quantitative measurement of Hg^{2+} was performed based on the formation of Os–Hg alloy. Os@ZIF-8 NCs had a wide detection range between 0 μM and 71.43 μM for Hg^{2+} with a limit of detection (LOD) of 2.29 μM. Using a MOF with a large surface area to load Os nanoparticles to achieve enhanced nanozyme activity is the novelty of this work.

1. Introduction

As a heavy metal, mercury is a common environmental pollutant due to its low degradation rate and high toxicity.[1,2] Ingested mercury can generate highly toxic methylmercury through methylation and accumulate in the brain through the blood–brain barrier.[3–5] Eventually, it results in neurological diseases such as spasms and epilepsy.[4,5] Thus, mercury poisoning is a big concern in our life. It is of great importance to detect mercury in water. So far, many analytical methods have been exploited to detect mercury, including atomic emission spectrometry (AES),[6] atomic absorption spectroscopy,[7] colorimetric methods,[8,9] fluorescence methods[10] and electrochemical methods.[2] Especially, colorimetric methods based on nanozymes have attracted lots of interest due to simplicity.[11]

Nanozymes are a class of nanomaterials with enzyme-like catalytic activity that have been applied in diverse fields, such as chemical,[12] biological sensing,[13] medical diagnosis[14] and environmental protection.[15] Especially, noble metal nanoparticles have attracted lots of interest due to the unique advantages of high catalytic activity, simple synthesis and good stability.[16] However, rarely has attention been paid to osmium nanoparticles. Osmium is a precious metal with low compressibility, high melting point and high bulk modulus.[17,18] Recent studies have revealed that Os nanozymes exhibited remarkable higher peroxidase-like activity and negligible oxidase-like activity in comparison with other noble metal-based nanozymes (*e.g.* Pt and Au).[19] This enabled Os-based NPs to be peroxidase-like specific nanozymes with high enzymatic activity. However, for practical applications, an issue still needs to be addressed. That is the easy aggregation of individual Os NPs, which may result in the decrease of the activity. Nanoparticles supported on metal–organic frameworks (MOFs) are a good choice to resolve this problem.[20] Especially, due to the advantages of large surface area, small pore size and easy preparation, zeolite imidazolate framework-8 (ZIF-8) has become a good candidate to support nanoparticles.[20–23] Inspired by this enlightenment, Os@ZIF-8 nanocomposites were designed and applied for detection of mercury.

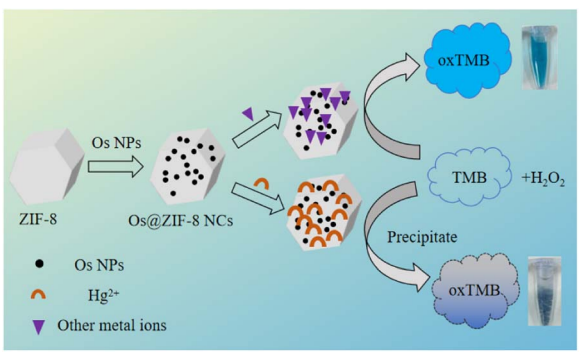

Scheme 1 Scheme illustration for the Os@ZIF-8 NCs preparation and detection of Hg^{2+} concentration.

School of Materials Science and Engineering, Yancheng Institute of Technology, Yancheng, 224051, China. E-mail: cuifengj123@163.com

† Electronic supplementary information (ESI) available. See DOI: https://doi.org/10.1039/d3ra08723a

Here, a Os@ZIF-8 NCs composite was prepared (Scheme 1). This nanocomposite has a large surface area and porous structure, which resulted in enhanced peroxidase-like activity. The steady-state kinetic and catalytic reaction kinetics were investigated. The high peroxidase-like activity was believed to originate from the strong binding between the nanocomposite and the substrate. The lower activation energy further explained the excellent catalytic ability. Using Os@ZIF-8 NCs as a probe, Hg^{2+} were detected with lower detection limit and wider linear range.

2. Experimental

2.1 Chemicals

K_2OsCl_6, $NaBH_4$ and terephthalic acid (TA) were purchased from Aladdin Industrial Corporation. 2-Methylimidazole, zinc acetate, hydrogen peroxide (98%), $CaCl_2$ and sodium acetate were purchased from Jiangsu Tongsheng Chemical Reagent Company. Acetate buffer was prepared by mixing glacial acetic acid and sodium acetate in proportion. 3,3′,5,5′-Tetramethylbenzidine (TMB), $CrCl_3$ were obtained from Sangon Biotech (Shanghai) Co., Ltd. Hg was purchased from National Testing Center for Nonferrous Metals and Electronic Materials. KCl, NaCl, $MgCl_2 \cdot 6H_2O$, $ZnCl_2$, $AlCl_3$, $CuCl_2 \cdot 2H_2O$, $FeCl_3$, $MnCl_2$ and glacial acetic were obtained from Sinopharm Chemical Reagent Co., Ltd. $PbCl_2$ was obtained from Shanghai Shisi Hewei Chemical Co., Ltd.

2.2 Preparation of Os@ZIF-8 NCs

0.015 mL K_2OsCl_6 (0.1 M) was added into 1 mL H_2O in a round bottom flask and stirred vigorously for 30 minutes at room temperature. Then, 0.1 mL $NaBH_4$ (0.2 M) prepared with ice water was slowly added into the mixture and stirred in dark for 90 minutes to obtain Os nanoparticles.

2 mL 2-methylimidazole (0.56 M) and 2 mL zinc acetate (70 mM) (prepared in methanol) were added into a round bottom flask and stirred for 24 hours at room temperature. Then, the obtained ZIF-8 was centrifuged and washed with methanol. The washed ZIF-8 was dissolved in methanol solution 5 mL (methanol : H_2O = 1 : 4). After that, 1 mL Os NPs was added into the above solution and stirred for 45 minutes. The mixture is allowed to stand for 24 hours to obtain Os@ZIF-8 NCs.

2.3 Characterization

The morphology and microstructure was observed and analyzed by transmission electron microscope (TEM, JEM-2100F) and an energy dispersive X-ray spectrometer (EDS, X-MaxN 80T IE250). X-ray photoelectron spectroscopy (XPS) measurement of the products was carried out using a ESCALAB 250Xi spectrometer. Fourier-transform infrared spectroscopy (FTIR) was recorded by using NEXUS-670. The surface area, pore volume, and pore size distribution of the catalysts were determined from N_2 adsorption–desorption isotherms using Beckman Coulter SA3100. XRD measurement was obtained by X-ray diffractometer (X'Pert3Powder). Size distribution of nanoparticles was obtained from the Malvern Zetasizer (Zetasizer Nano). Other characterization methods refer to our previous report.[24]

2.4 Enzyme-mimetic activities of Os@ZIF-8 NCs

The enzyme-mimic activities of Os@ZIF-8 NCs were evaluated by using TMB in the presence or absence of H_2O_2. Typically, in the absence or presence of 100 μL H_2O_2 (50 mM), 50 μL Os@ZIF-8 NCs, 100 μL TMB (8 mM) and 100 μL acetic acid buffer (50 mM, pH = 4.6) were mixed and spectra were measured after 10 min incubation at room temperature. After the enzyme-mimetic experiment, the mixture was centrifuged or under natural precipitation (by standing for 1.5 hours). Then, the recycling experiment was conducted by using the precipitate.

The steady-state kinetics of TMB oxidation were measured at room temperature with changes in the concentration of TMB (0, 0.1, 0.2, 0.5, 1, 2, 3, 4, 5, 6, 8 mM) with H_2O_2 fixed at 50 mM or H_2O_2 (0, 0.1, 0.5, 1, 5, 10, 20, 30, 40, 50 mM) with TMB fixed at 8 mM. The calculation is according to our previous literature.[24]

In the case of TA oxidation, 0.025 M TA was prepared in 0.1 M NaOH solution. Then, 20 μL TA (25 mM), 200 μL H_2O_2 (50 mM), 200 μL acetic acid buffer (pH = 4.6) and 100 μL Os@ZIF-8 NCs were incubated in 700 μL H_2O in the dark for 1 h. Finally, the fluorescence spectrum of the reaction mixture was collected.

2.5 Detection of Hg^{2+}

50 μL Hg with different concentrations were mixed with 50 μL Os@ZIF-8 NCs. Then, 100 μL TMB (8 mM), 100 μL H_2O_2 (50 mM), 100 μL acetate buffer (50 mM, pH = 4.6) and 300 μL deionized water were added and incubated for 5 min. Then, the obtained solution was measured for UV-vis absorption. For Hg^{2+} detection, the absorption value at 652 nm (characteristic peak for oxTMB) was used as the signal. Different concentration of Hg^{2+} gave different absorbance value. The curve of absorbance *versus* concentration could be fitted linearly, obtaining the calibration function. For selective experiments, 71.43 μM of other metal ions were added.

3. Results and discussion

3.1 Characterization of Os@ZIF-8 NCs

The detailed structural characteristics of Os@ZIF-8 NCs were investigated. Firstly, the morphology and microstructure of prepared nanomaterials was characterized by transmission electron microscopy (TEM). As showed in Fig. 1a, the original ZIF-8 exhibited hexagonal morphology. After deposition of Os NPs (Fig. 1b), it can be seen that Os NPs dispersed on the surface of ZIF-8. To further make clear the element distribution of Os@ZIF-8, EDS layered image and element mapping were employed. Fig. 1c indicates that the C, N and Zn elements from ZIF-8 were uniformly dispersed on the whole nanocomposite, while the Os element mainly distributed on the surface of ZIF-8. The EDS results in Fig. S1a† showed the presence of elemental C, N, Zn and Os, in accordance with the element mapping results. The size of the nanocomposite is mainly in the range of 450–600 nm as showed in Fig. S1b†

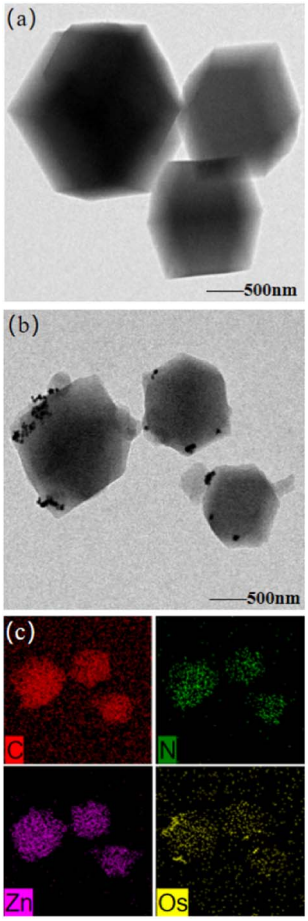

Fig. 1 Typical TEM images of (a) pristine ZIF-8, (b) Os@ZIF-8 NCs, (c) element mapping of Os@ZIF-8 NCs.

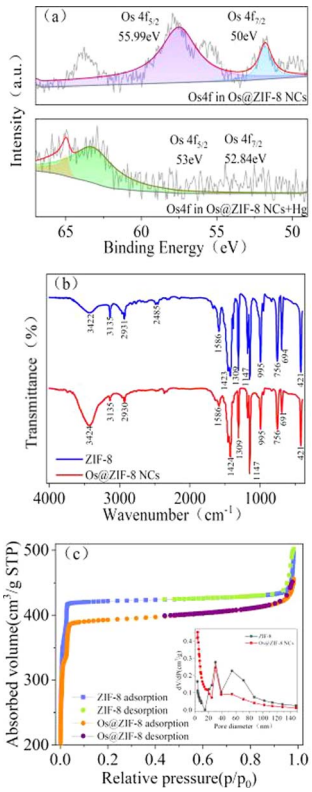

Fig. 2 (a) XPS spectra of the sample in: Os 4f regions of Os@ZIF-8 NCs and Os@ZIF-8 NCs + Hg^{2+}, (b) FTIR of ZIF-8 and Os@ZIF-8 NCs, (c) N_2 sorption isotherms and the pore size distribution plots (inset) of ZIF-8 and Os@ZIF-8 NCs.

X-ray photoelectron spectroscopy (XPS) analysis was performed to determine the oxidation state of Os in the composite. The binding energy of Os $4f_{7/2}$ and Os $4f_{5/2}$ appeared at 50 eV and 55.99 eV, which indicated the presence of Os^0 (Fig. 2a).[17,25] In order to analyze the structure of ZIF-8, FTIR spectra were measured. As showed in Fig. 2b, the characteristic peak stretching vibration of the C=N bond in the imidazole ring at 421 cm^{-1} and 1586 cm^{-1}, the planar bending of the imidazole ring near 1423 cm^{-1}, all kept the same for ZIF-8 and Os@ZIF-8 NCs. The results showed that Os NPs had no effect on the structure and functional groups of ZIF-8.

The permanent porosity of ZIF-8 was confirmed by reversible N_2 sorption experiments. Both ZIF-8 and Os@ZIF-8 NCs exhibited type-I adsorption isotherm behavior (Fig. 2c), with surface areas of 1425.94 $m^2\ g^{-1}$ and 1337.87 $m^2\ g^{-1}$ respectively. The BET surface areas value of ZIF-8 is similar to former reported value.[26] The pore volume are calculated to be 0.76 and 0.69 mL g^{-1} for ZIF-8 and Os@ZIF-8 NCs. Both the smaller surface area and pore volume of Os@ZIF-8 NCs further illustrate the distribution of Os NPs over the surface of ZIF-8. XRD measurement in Os nanoparticles, ZIF-8, Os@ZIF-8 NCs have been conducted. However, distinct characteristic peaks of Os were not observed neither in Os NPs nor in Os@ZIF-8 NCs. There was no significant change between ZIF-8 and Os@ZIF-8 NCs. The relative data has been added in Fig. S1c.†

3.2 Mimetics property of Os@ZIF-8 NCs

Combination of the nanozyme property of Os NPs and porous structure of ZIF-8, the prepared nanocomposites were expected to have broad application in nanocatalysis. The mimetic property of Os@ZIF-8 NCs was evaluated by employing chromogenic substrate TMB, which would turn to blue color in the appropriate catalyst. The results were showed in Fig. 3a, Os@ZIF-8 NCs + TMB + H_2O_2 system exhibited blue color and significant absorption at 652 nm, indicating the peroxidase-like activity of Os@ZIF-8 NCs. However, Os@ZIF-8 NCs + TMB displayed almost colorless. It indicates the Os@ZIF-8 NCs doesn't possess oxidase-like activity. In order to obtain the high catalytic activity, the experimental conditions were optimized. As shown in Fig. 3b–e, the optimal conditions were pH 4.6, H_2O_2 50 mM. TMB 8 mM, and 50 μL Os@ZIF-8 NCs. It is interesting that the optimal temperature for Os@ZIF-8 NCs was 60 °C (Fig. 3f), which was different from the previous reports that Os NPs exhibited very low peroxidase-like activity when the temperature was higher than 55 °C. It is possibly due to the stronger stability of Os under ZIF-8 loading.[27,28]

To make clear the exact catalytic mechanism of Os@ZIF-8 nanozyme, TA was chosen to conduct the related experiments

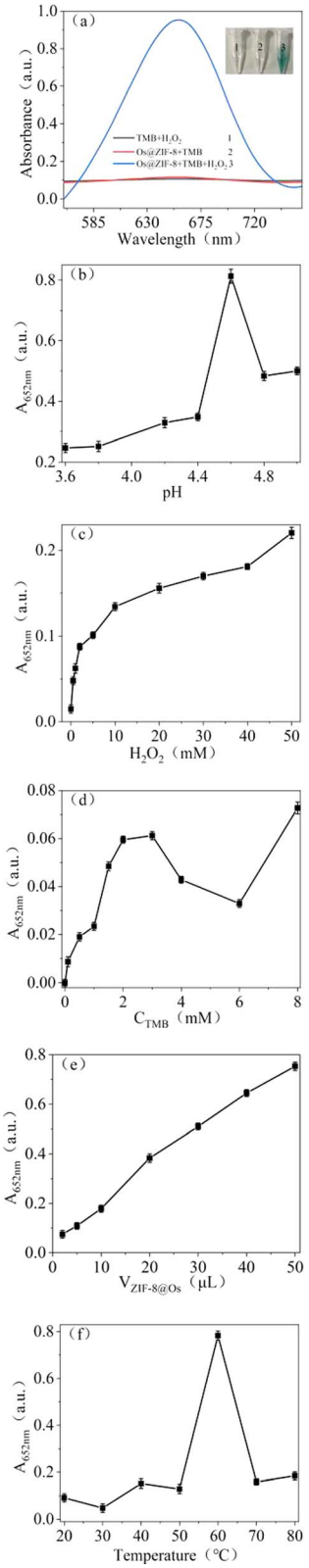

Fig. 3 (a) Absorption spectrum of TMB oxidation in the presence of different substances. Inset is the corresponding images. The effect of experimental conditions on the catalytic activity (b) pH, (c) H_2O_2 concentration, (d) TMB concentration, (e) the volume of Os@ZIF-8, (f) temperature.

because it could detect ˙OH free radicals.[29–31] As shown in Fig. S2,† in the TA oxidation experiment, fluorescence emission was observed after co-incubation of Os@ZIF-8 and H_2O_2, indicating the generation of ˙OH free radicals. The fluorescence intensity increased compared to TA + H_2O_2. However, the intensity of TA + H_2O_2 + Os@ZIF-8 NCs decreased compared to the TA + Os@ZIF-8 NCs. It is proposed that the quenching effect appeared in the presence of both Os@ZIF-8 NCs and H_2O_2.[32,33]

$$H_2O_2 \xrightarrow{Os@ZIF\text{-}8} OH^- + \cdot OH \quad (1)$$

$$\cdot OH + TMB \rightarrow oxTMB + OH^- \quad (2)$$

Two steps were involved in the catalytic process as shown in eqn (1) and (2). Firstly, ˙OH free radicals was generated from H_2O_2 in the presence of Os@ZIF-8. In this step, Os@ZIF-8 played the role of catalyst. Secondly, ˙OH free radicals oxidized TMB to oxTMB, accompanying the color change from colorless to blue. Totally, the peroxidase-like activity required both Os@ZIF-8 and H_2O_2, which can also be verified from Fig. 3a, where Os@ZIF-8 + TMB almost displayed colorless.

3.3 Kinetic analysis

The Michaelis–Menten equation describes the relationship of K_m, V_0 (initial velocity) and V_{max} (maximum velocity):

$$V_0 = \frac{V_{max}[S]}{K_m + [S]}$$

Lineweaver–Burk double reciprocal was obtained from Michaelis–Menten equation. The K_m and V_{max} could be calculated from Lineweaver–Burk double reciprocal. Smaller K_m indicates stronger binding, and *vice versa*.[34] As showed in Fig. 4a and b, the steady state kinetic of Os@ZIF-8 NCs followed Michaelis–Menten trend. The K_m and V_{max} were obtained from the Lineweaver–Burk double reciprocal (Fig. 4c and d). To further analyze the mimicking property of Os@ZIF-8 NCs, the steady-state kinetic analysis of pure Os NCs was conducted and presented in Fig. S3.†

As listed in Table 1, Os@ZIF-8 NCs displayed much smaller K_m for TMB and H_2O_2 compared to pure Os NPs. Zeta potential of Os and Os@ZIF-8 were measured to be −26 mV and 14 mV. Considering the positive property of TMB, Os NPs was supposed to have stronger binding to TMB. However, the result was different. This phenomenon indicates other factors showed intense effect on the catalytic activity. It is speculated that two reasons are responsible for the result. On one hand, the porous structure of ZIF-8 could exhibit confinement effect for contact of Os NPs and substrate. This hypothesis could be verified from Fig. 2d. The average pore size of Os@ZIF-8 NCs is smaller than ZIF-8 due to a mount of Os distributed on the pore. On the other hand, the large surface area of Os@ZIF-8 NCs may be more easily to absorb substrate molecules. In addition, compared with other nanozymes, such as GSH-AgNPs,[35] Fe_3O_4 NPs,[36] Cu@Au/Pt[24] and $Cu(OH)_2$ SCs,[37] Os@ZIF-8 NCs also displayed smaller K_m for TMB. All these data indicated the excellent peroxidase-like activity of prepared nanocomposites.

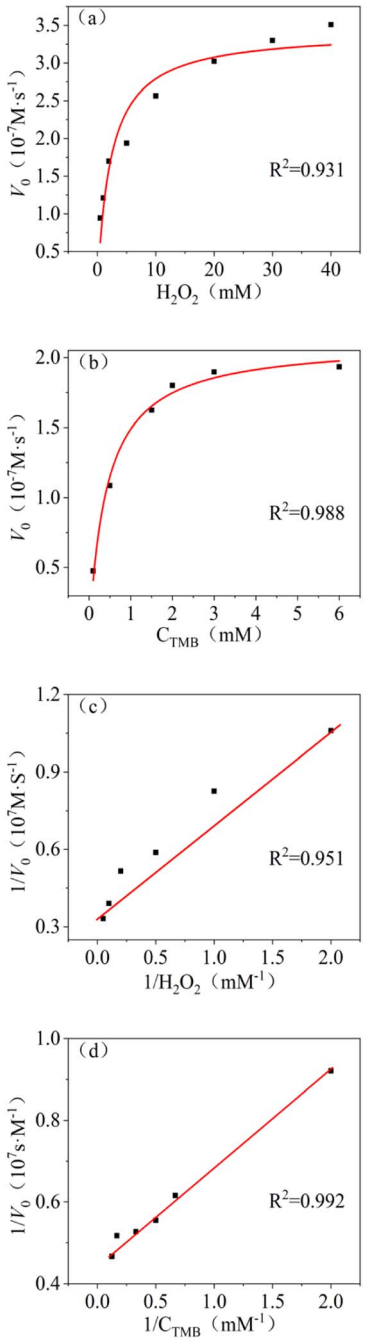

Fig. 4 Steady-state kinetic analysis with Os@ZIF-8 NCs, Michaelis–Menten trend of (a) H_2O_2 and (b) TMB, Lineweaver–Burk plot of (c) H_2O_2 and (d) TMB.

In the reaction from TMB to oxTMB, Os@ZIF-8 NCs played the role of catalyst. Therefore, the activation energy is another important parameter to understand the catalytic reaction. Fig. S4† displays the experimental results obtained from three different temperature (20 °C, 40 °C, 50 °C). It can be seen, the absorbance at 652 nm increased with time for both Os NPs and Os@ZIF-8 NCs at each temperature. After that, it reached a plateau, indicating the accomplishment of the reaction from TMB to oxTMB. The first-order kinetics for the oxidation of TMB could be applied to our system. As shown in Fig. 5a–c, the ln(A/A_0) (the initial absorption value at 652 nm was A_0, the absorption value at t time was A) is linearly to time. According to the linear relationship, the average reaction rate constant (k) for both catalyst at three temperature were calculated and listed in Table S1.† Moreover, based on the Arrhenius equation $\ln k = \ln A - E_a/RT$ and the linear fitting of $\ln k$ *versus* $1/T$ (Fig. 5d), the apparent activation energy (E_a) were obtained. The activation energy of Os@ZIF-8 NCs (57.58 kJ mol^{-1}) is lower than that of Os NPs (391.67 kJ mol^{-1}), implying a better catalytic activity for Os@ZIF-8 NCs. It is probably due to the confinement effect of ZIF-8 for contact of Os NPs and substrates.[25] "Confinement effects" mainly related to three aspects. One is containment of catalyst (Os@ZIF-8) and substrate (TMB) in the same space. The other is the inhibition of catalyst aggregation. The third is protecting the reaction between Os@ZIF-8 and TMB from exposure to potentially deleterious substances.[38]

Table 1 Comparison of the apparent Michaelis–Menten constant (K_m) and maximum reaction rate (V_{max})

Catalyst	Substrate	K_m (mM)	V_{max} (10^{-7} M s^{-1})	Ref.
GSH-AgNPs	H_2O_2	58.6	2.15	35
	TMB	4.17	24.7	
Fe_3O_4 NPs	H_2O_2	0.16	0.18	36
	TMB	1.372	0.419	
Cu@Au/Pt	H_2O_2	8.54	2.43	24
	TMB	6.64	6.14	
$Cu(OH)_2$ SCs	H_2O_2	0.199	4.251	37
	TMB	2.488	4.483	
Os NPs	H_2O_2	27.342	43.197	This work
	TMB	1.53	6.585	
Os@ZIF-8 NCs	H_2O_2	0.516	2.21	This work
	TMB	0.926	2.5776	

3.4 Recycling experiment

Recyclability is another important factor for application of nanozyme. Therefore, recycling experiments were conducted on the prepared pure Os NPs and Os@ZIF-8 NCs. Natural precipitation and centrifugation were used to evaluate the recycle effect. The results in Fig. 6a showed that the activity of pure Os NPs and precipitated Os@ZIF-8 NCs deceased to 60% after twice recycle. However, the activity of centrifuged Os@ZIF-8 NCs remained 90%. It was possible that during natural precipitation, some samples may not precipitate thoroughly enough, resulting in some losses. After 4 times recycle, the activity of precipitated and centrifuged Os@ZIF-8 NCs are 22.93% and 19.57%, respectively. However, the activity of pure Os NPs is only 8.44%. It is proposed that the centrifugation of Os NPs can't separate all the nanoparticles due to their small size. The same trend was observed for 5 times recycle. In a word, Os@ZIF-8 NCs could maintain higher activity compared to pure Os NPs after recycling experiments.

3.5 Detection of Hg^{2+}

To explore the application of Os@ZIF-8 NCs, quantitatively detection of Hg^{2+} was performed under optimized condition.

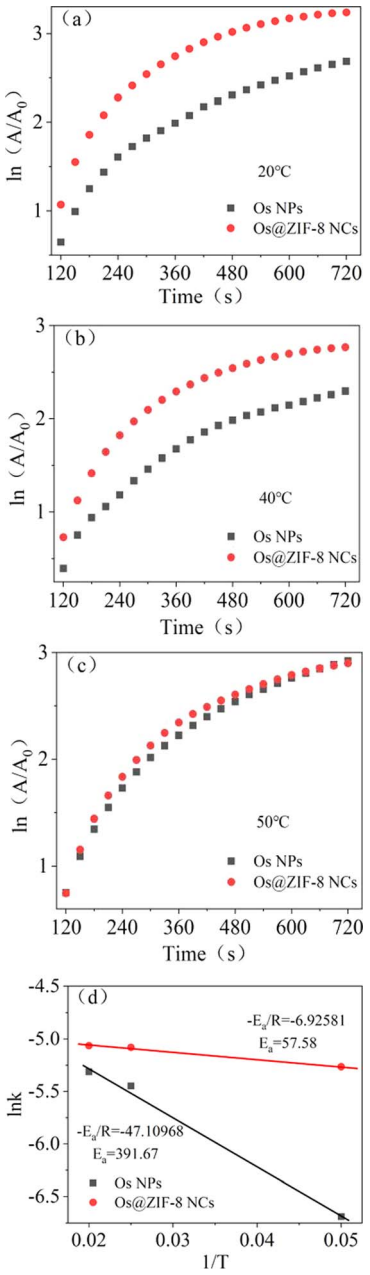

Fig. 5 (a)–(c)The Arrhenius plots for reactions catalyzed by Os NPs and Os@ZIF-8 NCs, (d) the activation energies (E_a) can be calculated from the slope of the linear fitting.

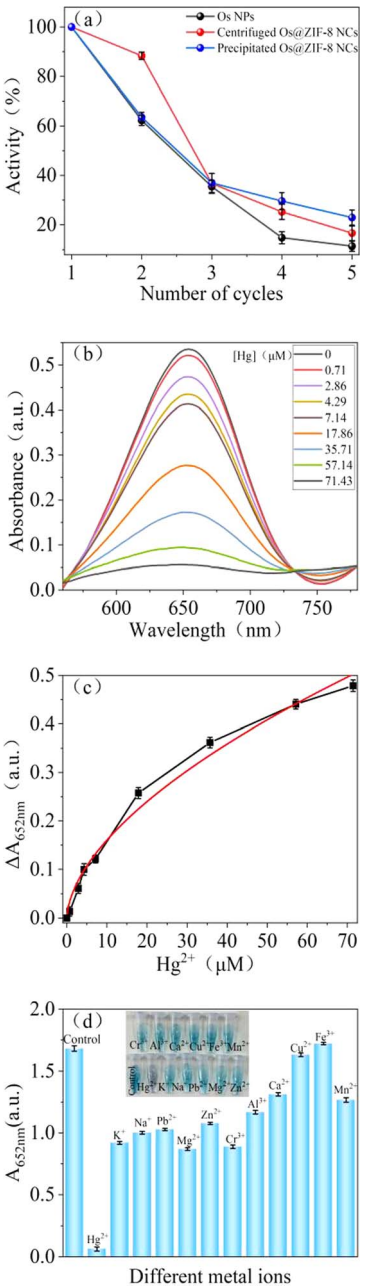

Fig. 6 (a) Activity of pure Os NPs and Os@ZIF-8 NCs in the recycling experiment; (b) UV-vis spectra and (c) ΔA at 652 nm with different concentration of Hg^{2+} and its linear fitting diagram; (d) absorption values at 652 nm with different metal ions.

Fig. 6b demonstrates the effect of Hg^{2+} concentration on the peroxidase-like activity of Os@ZIF-8 NCs. It can be seen that as the concentration of Hg^{2+} increases, the absorption value at 652 nm decreases. Fig. 6c shows that ΔA at 652 nm *versus* concentration of Hg^{2+} ($\Delta A = A_0 - A$, where A_0 and A are absorption intensities at 652 nm in the absence and presence of Hg^{2+}, respectively). It can be seen that the absorbance exhibits a nonlinear variation between 0 and 71.43 μM. However, 0–17.86 μM and 17.86–71.43 μM showed linear relationship, respectively. The limit of detection (LOD) was calculated to be 2.29 μM according to the rule of $3\sigma/S$, σ represents the standard deviation of the sample, and S represents the slope of the sample. Table 2 lists the detection limits and detection ranges of other materials for detecting Hg^{2+}. It can be seen that Os@ZIF-8 NCs has a wide range and low detection limit compared with other materials. It is worth to mention, the black flocculent generated upon addition of Hg^{2+}were collected for XPS analysis. As showed in Fig. 2a, the two peaks for Os $4f_{7/2}$ (50 eV) and Os $4f_{5/2}$ (55.99 eV) disappeared, while a new peak at 63 eV appeared. It was reported binding energy of Hg^0 at 100.7 and 104.7 eV.[39] The new peak located between Os^0 and Hg^0, which indicated the formation of Os–Hg alloy.

Table 2 Comparison of other materials for the detection of Hg^{2+}

Materials	Linear range (μM)	LOD	Ref.
ZIF-8@MnO_2	0.05–10	100 nM	5
GNPs	1–20	1.09 μM	40
SAC	10–50	12.6 μM	41
CDs	4–18	2.47 μM	42
MOF-macroporous carbon composite	0.25–3.5	50 nM	43
Os@ZIF-8 NCs	0–71.43	2.29 μM	This work

Then, the influence of nanocomposite on the detection of Hg^{2+} was evaluated. Firstly, Os@ZIF-8 NCs have long-term storage stability and can be ultrasonically dispersed upon reuse. The activity of Os@ZIF-8 NCs with storage days was added in Fig. S5a.† It can be seen, the activity almost unchanged even after one day storage. However, the activity decreased sharply after one day. Therefore, Os@ZIF-8 NCs could be used in one day for Hg^{2+} detection to get good sensitivity. Moreover, the response time of the nanocomposite for Hg^{2+} detection was showed in Fig. S5b.† The absorbance tended to stabilize at 300 seconds. Therefore, 5 minutes was chosen as the response time for testing. In addition, we also investigated the influence of temperature on the detection of Hg^{2+}. As shown in Fig. S6,† the trend was similar under the three temperatures (20 °C, 35 °C, 50 °C), so the influence of temperature on the detection of Hg^{2+} was negligible.

In addition, to evaluate whether other metal ions will affect the detection, selective experiments were conduct. 71.43 μM of K^+, Na^+, Mg^{2+}, Pb^{2+}, Zn^{2+}, Cr^{3+}, Al^{3+}, Cu^{2+}, Ca^{2+}, Fe^{3+}, Mn^{2+} were used to perform selectivity experiment. As shown in Fig. 6d, the solution color with Hg was lighter than with other metal ions. Meanwhile, there is almost no absorption peak upon addition of Hg^{2+}. The absorption value at 652 nm for all the metal ions was summarized in Fig. 6d. It is clear that the value is much lower for Hg^{2+} than other metal ions. Fig. 6d shows that the nanocomposite is not specific for Hg^{2+} detection. However it is more sensitive to Hg^{2+}. Nitrogen of ZIF-8 has lone pairs of electrons, which could form coordination bond with metal ions. The coordination compound perhaps blocked the active site of Os NPs, resulting decrease of catalytic ability. However, the binding force between Hg^{2+} and ZIF-8 is much stronger compared to other metal ions. Therefore, it is more sensitive to Hg^{2+}.

4. Conclusions

In summary, we have successfully deposited Os NPs on the surface of ZIF-8. Enhanced peroxidase-like activity verified as stronger binding to TMB and H_2O_2 was achieved thanks to the confinement effect and large surface area that ZIF-8 provided. Importantly, Os@ZIF-8 NCs had smaller activation energy compared to Os NPs, further verifying the better catalytic ability. Moreover, Os@ZIF-8 NCs exhibited better recoverability. In addition, the nanocomposite provided a sensitive approach for selective detection of Hg^{2+}. It is supposed to be widely applied in water pollution.

Conflicts of interest

The authors declared that they have no conflicts of interest to this work.

Acknowledgements

This work was supported by Natural Science Foundation of China (21605128).

Notes and references

1 A. Hu, G. Chen, A. Huang, Z. Cai, T. Yang, C. Ma, L. Li, H. Gao, J. Gu, C. Zhu, Y. Wu, X. Qiu, J. Xu, J. Shen and L. Zhong, *J. Fluoresc.*, 2023, **34**, 905–913.
2 L. Huang, Y. Cao and D. Diao, *Sens. Actuators, B*, 2020, **305**, 127495.
3 K. Abbas, H. Znad and M. R. Awual, *Chem. Eng. J.*, 2018, **334**, 432–443.
4 T. A. Saleh, G. Fadillah, E. Ciptawati and M. Khaled, *TrAC, Trends Anal. Chem.*, 2020, **132**, 116016.
5 N. Liang, X. Ge, Y. Zhao, L. Xia, Z.-L. Song, R.-M. Kong and F. Qu, *J. Hazard. Mater.*, 2023, **454**, 131455.
6 R. Wang and W.-X. Wang, *Environ. Pollut.*, 2018, **234**, 288–296.
7 V. A. Lemos and L. O. dos Santos, *Food Chem.*, 2014, **149**, 203–207.
8 D. Zhang, S. Yang, Q. Ma, J. Sun, H. Cheng, Y. Wang and J. Liu, *Food Chem.*, 2020, **313**, 126119.
9 S. Zhang, H. Li, Z. Wang, J. Liu, H. Zhang, B. Wang and Z. Yang, *Nanoscale*, 2015, **7**, 8495–8502.
10 H. Wang, X. Wang, M. Liang, G. Chen, R.-M. Kong, L. Xia and F. Qu, *Anal. Chem.*, 2020, **92**, 3366–3372.
11 J. Dai, L. Wang, F. Xu and G. Ma, *Ionics*, 2022, **28**, 5251–5255.
12 Q. Yang, Y.-Y. Mao, Q. Liu and W.-W. He, *Rare Met.*, 2023, **42**, 2928–2948.
13 M. Feng, X. Li, X. Zhang and Y. Huang, *TrAC, Trends Anal. Chem.*, 2023, **166**, 117220.
14 X. Zhang, X. Chen and Y. Zhao, *Nano-Micro Lett.*, 2022, **14**, 95.
15 J. Venkatesan, P. K. Gupta, S. E. Son, W. Hur and G. H. Seong, *J. Cluster Sci.*, 2022, **34**, 23–43.
16 W. Shou, S.-T. Yang, Y.-L. Wang and L.-H. Guo, *Chin. J. Anal. Chem.*, 2021, **49**, 676–685.
17 S. B. He, M. T. Lin, L. Yang, H. A. A. Noreldeen, H. P. Peng, H. H. Deng and W. Chen, *ACS Appl. Mater. Interfaces*, 2021, **13**, 44541–44548.
18 S. B. He, Q. Q. Zhuang, L. Yang, M. Y. Lin, Y. Kuang, H. P. Peng, H. H. Deng, X. H. Xia and W. Chen, *Anal. Chem.*, 2020, **92**, 1635–1642.
19 M. Gerami, H. Farrokhpour and N. Orangi, *J. Phys. Chem. A*, 2023, **127**, 3991–4004.
20 X. Wang, R. Xu, Y. Tian, X. Gao, W. Zhang, Z. Sun, Y. Mou, X. Sun, Y. Guo and F. Li, *Sens. Actuators, B*, 2023, **388**, 133856.

21 F. K. Arabbani, D. Vasu, S. Sakthinathan, T. W. Chiu and M. C. Liu, *Electroanalysis*, 2023, **35**, e202200284.
22 Y. Xie, X. Dong, N. Cai, F. Yang, W. Yao and L. Huang, *Foods*, 2023, **12**, 813.
23 Y. Guo, J. Zhang, J. Liu, N. Wang and X. Su, *Anal. Chim. Acta*, 2023, **1276**, 341649.
24 C. Jiang, X. Wei, S. Bao, H. Tu and W. Wang, *RSC Adv.*, 2019, **9**, 41561–41568.
25 R. L. Papporello, E. E. Miró and J. M. Zamaro, *Microporous Mesoporous Mater.*, 2015, **211**, 64–72.
26 Y. Wang, F. Wang and J. Zhang, *Cryst. Growth Des.*, 2019, **19**, 3430–3434.
27 S. He, L. Yang, P. Balasubramanian, S. Li, H. Peng, Y. Kuang, H. Deng and W. Chen, *J. Mater. Chem. A*, 2020, **8**, 25226–25234.
28 X. Cui, J. Zhang, Y. Liu, W. Shao, Y. Tang and H. Sun, *ChemNanoMat*, 2023, **9**, DOI: **10.1002/cnma.202300310**.
29 Z. Fu, W. Zeng, S. Cai, H. Li, J. Ding, C. Wang, Y. Chen, N. Han and R. Yang, *J. Colloid Interface Sci.*, 2021, **604**, 113–121.
30 X. Jiang, P. Gray, M. Patel, J. Zheng and J. J. Yin, *J. Mater. Chem. B*, 2020, **8**, 1191–1201.
31 B. Han, H. Guan, B. Peng, Y. Zhang and Y. Liu, *Anal. Methods*, 2022, **14**, 4832–4841.
32 X. Liu and F. Liu, *Carbohydr. Polym.*, 2023, **310**, 120726.
33 H. M. Abdul Hakkeem, A. Babu, N. Shilpa, A. A. Venugopal, A. P. Mohamed, S. Kurungot and S. Pillai, *Carbohydr. Polym.*, 2022, **292**, 119723.
34 L. Ou, T. L. Herzog, C. M. Wilmot and C. B. Whitley, *Mol. Genet. Metab.*, 2014, **111**, 113–115.
35 C. Jiang, Z. Bai, F. Yuan, Z. Ruan and W. Wang, *Spectrochim. Acta, Part A*, 2022, **265**, 120348.
36 N. Bagheri, A. Khataee, J. Hassanzadeh and B. Habibi, *Spectrochim. Acta, Part A*, 2019, **209**, 118–125.
37 J. Mu, J. Li, X. Zhao, E.-C. Yang and X.-J. Zhao, *Sens. Actuators, B*, 2018, **258**, 32–41.
38 S. Karmakar, S. Barman, F. A. Rahimi and T. K. Maji, *Energy Environ. Sci.*, 2021, **14**, 2429–2440.
39 R. Chadha, A. Das, A. K. Debnath, S. Kapoor and N. Maiti, *Colloids Surf., A*, 2021, **615**, 126279.
40 N. Zohora, D. Kumar, M. Yazdani, V. M. Rotello, R. Ramanathan and V. Bansal, *Colloids Surf., A*, 2017, **532**, 451–457.
41 Y.-C. Hsieh, J.-L. Chir, S.-T. Yang, S.-J. Chen, C.-H. Hu and A.-T. Wu, *Carbohydr. Res.*, 2011, **346**, 978–981.
42 F. Yan, D. Kong, Y. Luo, Q. Ye, J. He, X. Guo and L. Chen, *Microchim. Acta*, 2016, **183**, 1611–1618.
43 K. Jia, K. Yi, W. Zhang, P. Yan, S. Zhang and X. Liu, *Sens. Actuators, B*, 2022, **370**, 132443.